Preprint manuscript

Prepared for Journal Submission

The Tocantins Framework: A Machine Learning-Based Assessment of Intra-urban Thermal Anomalies

Isaque Carvalho Borges
EcoAção Brasil,
Palmas, Tocantins, Brazil.

Johari A. Barrientos-Murray
EcoAção Brasil,
Cáceres, Extremadura, Spain.

Lucca Pereira da Cunha
EcoAção Brasil,
São Paulo, São Paulo, Brazil.

Isabela Nunes Toniolo
EcoAção Brasil,
Abuja, Federal Capital Territory, Nigeria.

Corresponding author: isaque@ecoacaobrasil.org

The Tocantins Framework: A Machine Learning-Based Assessment of Intra-urban Thermal Anomalies

Abstract

The Urban Heat Island (UHI) effect has been extensively studied at the city scale. Yet, the Intra-Urban Heat Island and the Intra-Urban Cool Island effects remain poorly characterized due to the absence of standardized quantification frameworks. This study introduces the Tocantins Framework, a dual-metric system combining machine learning and spatial morphology to identify and quantify intra-urban thermal anomalies in Landsat imagery. The framework consists of two metrics: the Impact Score (IS), which assesses the spatial extent and thermal intensity of Extended Anomaly Zones (EAZs), and the Severity Score (SS), which quantifies core thermal anomalousness.

A two-stage detection methodology first identifies statistical temperature extremes (2nd and 98th percentiles), then applies Random Forest regression to distinguish pixels exhibiting thermally anomalous behavior unexplained by spectral indices (NDVI, NDWI, NDBI, NDBSI). The model achieved $R^2 = 0.8023$ (RMSE = 1.1612°C) when predicting Land Surface Temperature (LST) from spectral properties. We capture residual variance for anomaly detection.

When applied to a Landsat 8 composite from the first semester of 2025 for Palmas, Tocantins, Brazil, the framework identified 103 thermal anomalies (76 IUHIs and 27 IUCIs) covering 30.42 km^2 of the urban area. Impact Scores ranged from −14.69 to 13.32 and Severity Scores from −14.49 to 16.87. The two metrics showed a weak correlation ($R^2 = 0.154$), confirming they capture complementary and distinct aspects of anomaly phenomena.

The framework provides a reproducible, open-source methodology for evidence-based urban heat mitigation planning, enabling practitioners to identify priority intervention areas based on both thermal intensity and spatial impact. The complete implementation is available as a Python package via PyPI.

Keywords— Tocantins Framework, Impact Score, Severity Score, Machine Learning, Artificial Intelligence, Urban Heat Islands, Urban Cool Islands, Intra-urban Thermal Anomalies

Introduction

The Urban Heat Island (UHI) effect is defined as the phenomenon where urban areas exhibit higher temperatures than their surrounding rural areas, primarily due to human activities and urban infrastructure altering the natural landscape and heat storage dynamics (Oke, 1982).

On the other hand, the Intra-urban Heat Island effect (IUHI), also named as the Micro-urban Heat Island effect (MUHI), despite not having a standard definition, refers to the microclimatic phenomenon where specific locations experience higher surface temperatures compared to their neighbouring areas within the same city (Aniello et al., 1995). In other words, whereas the analysis of UHIs emphasizes city-wide temperature variations, the study of IUHIs investigates fine-scale spatial variabilities of heat within the same urban environment (Aucoin et al., 2022).

Concomitantly, Intra-urban Cool Islands (IUCIs), also referred to as Micro-urban Cool Islands (MUCIs), describe localized areas within a city that exhibit lower temperatures compared to their neighboring urban surroundings. In general terms, IUCIs are typically associated with increased vegetation, urban morphology, and reduced solar heat gain (Yang et al., 2017; Wong & Yu, 2005).

These microclimatic phenomena result from localized deviations in the urban thermal field caused by surface heterogeneities. For instance, parks and gardens often radiate less heat than other areas, such as parking lots or concrete buildings (Aram et al., 2019; Chen et al., 2022; Onishi et al., 2010; Wang et al., 2017). Consequently, a thorough investigation of IUHIs and IUCIs is necessary to advance the understanding of environmental inequity, often linked to geospatial heterogeneity, including issues such as urban segregation and unequal access to heat mitigation resources such as vegetation, shade, or cooling infrastructure (Chen, 2024; Hsu et al., 2021; Li et al., 2024; Mazzone et al., 2024).

Additionally, as noted by Aucoin et al. (2022), the study of such hyperlocalized heat variations is relevant for facilitating the identification of specific urban locations that actively contribute to climatic discomfort and pose significant risks to human health. However, despite their relevance, IUHIs and IUCIs are considerably understudied and lack a comprehensive framework of analysis.

To address the fragmented and inconsistent study of these micro-urban thermal anomalies, this work introduces the Tocantins Framework, a dual-metric system developed to quantify intra-urban heat and cool anomalies. The framework comprises two complementary scores: the Impact Score (IS), which quantifies the thermo-spatial influence of an anomaly on its surrounding environment, and the Severity Score (SS), which quantifies the thermal anomalousness of the anomaly core itself. This approach offers a standardized framework for identifying areas that deviate from expected thermal conditions within the urban landscape, facilitating comparative analysis across neighborhoods and cities and supporting evidence-based urban planning and heat mitigation strategies.

Methods

Data Acquisition

This study used the Landsat data archive, specifically the Collection 2 Level-2, accessed and processed through the Google Earth Engine (GEE) cloud-computing platform. Since the analysis covers the time frame between 1985 and 2025, data from three generations were collected: Landsat 5 Thematic Mapper (TM), Landsat 7 Enhanced Thematic Mapper Plus (ETM+), and Landsat 8/9 Operational Land Imager/Thermal Infrared Sensor (OLI/TIRS). The methods related to data collection and pre-processing were standardized within the GEE environment to ensure consistency across all Landsat sensors.

The initial area of interest was defined as the administrative boundary of the municipality of Palmas, in the Brazilian state of Tocantins, based on the division proposed by the UN Food and Agriculture Organization, through the Global Administrative Unit Layers dataset.

Cloud masking for Landsat scenes was performed using the pixel quality assessment band, which is derived from the CFMask/Fmask provided with Landsat Collection-2 Level-2 products. This process involved excluding pixels flagged as cloud or cloud-shadow across all sensors. Additionally, for imagery where the cirrus band is available (i.e., Landsat 8/9), pixels flagged as cirrus were also excluded. Median composites for six-month intervals of the masked scenes were then generated to create robust, cloud-free images for analysis.

Radiometric Scaling and Spectral Indices Calculation

The Landsat Collection 2 Level-2 surface reflectance data product is stored in a 16-bit integer format with values ranging from 0 to 65535. For this reason, a scaling factor provided in the product documentation was passed into each band's surface reflectance pixel values (PV) to convert unsigned integers to float values representing surface reflectance in physically meaningful units (United States Geological Survey, 2022):

$$\text{Surface Reflectance} = 0.0000275 PV - 0.2 \tag{1}$$

Similarly, a scaling function was also applied to the thermal band (United States Geological Survey, 2022), resulting in land surface temperatures in Kelvin:

$$T_{\mathrm{K}} = 0.00341802 PV + 149 \tag{2}$$

The surface temperature was then converted to the Celsius scale:

$$T_{\mathrm{C}} = T_{\mathrm{K}} - 273.15 \tag{3}$$

Subsequently, four spectral indices were calculated to characterize land cover properties. Band numbers correspond to Landsat 8/9 OLI sensor.

NDVI (Normalized Difference Vegetation Index): NDVI quantifies vegetation density and health by measuring the difference between near-infrared (NIR) and red (R) reflectance. Healthy vegetation strongly absorbs red light for photosynthesis while reflecting NIR radiation through leaf structure (Tucker, 1979):

$$\text{NDVI} = \frac{\text{NIR (Band 5)} - \text{Red (Band 4)}}{\text{NIR (Band 5)} + \text{Red (Band 4)}} \tag{4}$$

NDWI (Normalized Difference Water Index): NDWI measures water content in vegetation and soil by exploiting the contrast between green and NIR reflectance. Water absorbs strongly in NIR wavelengths while reflecting in green (Gao, 1996):

$$\text{NDWI} = \frac{\text{Green (Band 3)} - \text{NIR (Band 5)}}{\text{Green (Band 3)} + \text{NIR (Band 5)}} \tag{5}$$

NDBI (Normalized Difference Built-up Index): NDBI identifies urban built-up areas by measuring the difference between shortwave infrared (SWIR) and NIR reflectance. Built-up surfaces exhibit higher SWIR reflectance than vegetated areas (Zha et al., 2003):

$$\text{NDBI} = \frac{\text{SWIR1 (Band 6)} - \text{NIR (Band 5)}}{\text{SWIR1 (Band 6)} + \text{NIR (Band 5)}} \tag{6}$$

NDBSI (Normalized Difference Bare Soil Index): NDBSI identifies exposed soil and barren land by combining multiple spectral bands. Bare soil exhibits characteristic reflectance in red and SWIR wavelengths with low reflectance in NIR and blue (Deng et al., 2018):

$$\text{NDBSI} = \frac{(\text{SWIR1 (Band 6)} + \text{Red (Band 4)}) - (\text{NIR (Band 5)} + \text{Blue (Band 2)})}{(\text{SWIR1 (Band 6)} + \text{Red (Band 4)}) + (\text{NIR (Band 5)} + \text{Blue (Band 2)})} \tag{7}$$

Study Area and Spatial Delimitation

The municipality of Palmas, Tocantins, consists of a compact urban center surrounded by a vast non-urban area. According to the Brazilian Institute of Geography and Statistics (IBGE), in 2019, the urbanized area accounts for only approximately 5% of the municipality's total area (IBGE, 2019).

Rural and densely vegetated areas typically exhibit decreased temperatures due to higher evapotranspiration rates, while urban surfaces accumulate and retain heat through materials with high thermal mass and exposed soil (Oke, 1982). Hence, including the non-urban territory in this intra-urban study would bias our analysis and prevent accurate identification of micro-urban heat and cool islands.

To address this impasse, we delineated a spatial subset highlighting the urbanized portion of Palmas (Figure 1). This polygon was manually digitized based on visual interpretation of Landsat imagery and excludes isolated rural settlements and non-anthropized areas.

The effect of this delineation is apparent when comparing the thermal characteristics of the urban polygon against the entire municipality. Figure 2 directly illustrates this contrast, plotting the land surface temperature (LST) distribution for both areas throughout 40 years.

Whereas the delineated urban polygon exhibits a mean LST of 35.22°C and a standard deviation of 5.33°C, the mean LST of the broader Palmas is 32.48°C, with a 5.09°C deviation. This discrepancy is visually represented in the graph by the distinct rightward shift of the urban area's (magenta) distribution curve, confirming the presence of a significant Urban Heat Island (UHI) effect. The municipality's overall cooler profile (blue curve) is clearly dominated by the thermal signature of its vast non-urban and vegetated territories, validating the initial hypothesis.

Beyond quantifying this municipality-wide UHI, the spatial delimitation serves a more critical purpose. Isolating the urban polygon removes the significant cooling bias from the surrounding

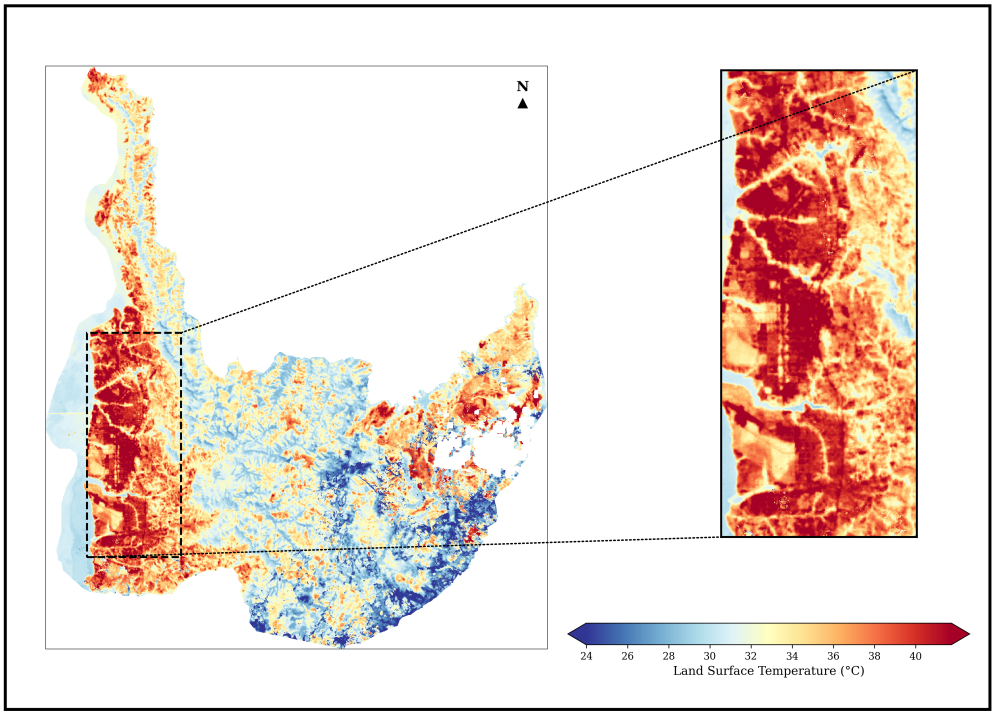

Figure 1: Selected urban polygon featuring the urban area of Palmas.

non-anthropized landscape. This step enables the study to focus on its primary objective: a high-resolution analysis of intra-urban thermal anomalies, specifically the localized micro-heat islands and cool islands that define the city's internal thermal landscape.

Anomaly Detection

The identification of intra-urban thermal anomalies was performed through a dual-stage approach combining statistical thresholding with machine learning-based residual analysis. This methodology enables the detection of pixels that exhibit thermal behavior that significantly deviates from expected patterns based on their spectral characteristics.

First, the initial anomaly candidates were identified using percentile-based statistical thresholds applied to the land surface temperature distribution. These thresholds were chosen based on the

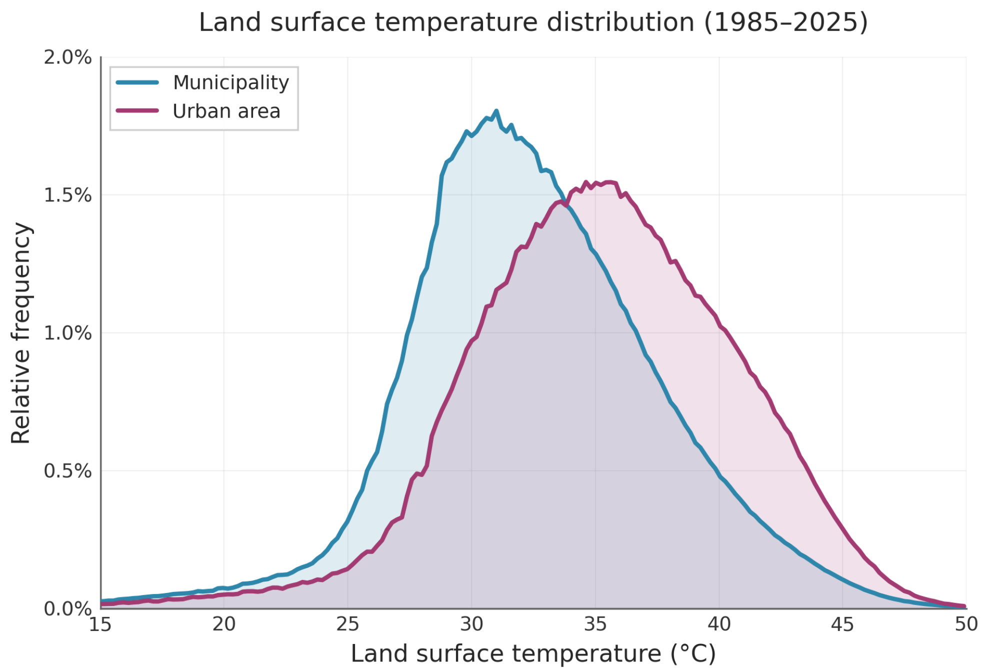

Figure 2: Comparative distribution of land surface temperatures in the municipality and in the selected urban polygon.

work by Aucoin et al. (2022), where surface temperatures that roughly corresponded to two standard deviations below and above the mean were considered thermally anomalous relative to the city's internal baseline. Therefore, pixels with LST values falling below the 2nd percentile (P_2) or above the 98th percentile (P_{98}) were flagged as potential cold and hot anomalies, respectively:

$$M_1^{\text{cold}} = \{(i, j) \mid \text{LST}_{i,j} \leq P_2\} \tag{8}$$

$$M_1^{\text{hot}} = \{(i, j) \mid \text{LST}_{i,j} \geq P_{98}\} \tag{9}$$

where M_1^{cold} and M_1^{hot} represent the binary masks of statistically identified cold and hot anomalies, and (i, j) denotes a pixel.

This preliminary approach captures extreme thermal values while maintaining robustness against outliers and variations in the overall temperature distribution across different time periods and atmospheric conditions. However, to refine the statistical anomalies and account for thermal variations driven by land cover characteristics, a Random Forest regression model was trained to predict LST from spectral indices.

The model was trained exclusively on non-anomalous pixels, that is, those not included in either M_1^{cold} or M_1^{hot}, to establish a local reference relationship between surface properties and thermal behavior:

$$\hat{T}_{\text{LST}} = f_{\text{RF}}(\text{NDVI}, \text{NDWI}, \text{NDBI}, \text{NDBSI}) \tag{10}$$

where $\hat{T}_{\text{LST}}$ represents the predicted LST and f_{RF} denotes the trained Random Forest model. The Random Forest algorithm was configured with 100 estimators, a maximum depth of 20, a minimum samples per split of 10, and a minimum samples per leaf of 5. These parameters were selected to balance complexity and generalization, preventing model overfitting while maintaining sufficient capacity to capture nonlinear relationships between spectral indices and thermal response.

This machine learning-based step is crucial for transitioning from identifying absolute thermal extremes (via P_2/P_{98}) to detecting contextual thermal anomalies. Since spectral indices serve as proxies for multifaceted land cover characteristics, modeling the relationship between them and LST establishes a predicted baseline for every pixel.

LST residuals (ΔT) were then calculated as the difference between observed and predicted temperatures:

$$\Delta T_{i,j} = \text{LST}_{i,j} - \hat{T}_{\text{LST}_{i,j}} \tag{11}$$

Positive residuals indicate pixels warmer than expected based on the predicted values from their spectral properties, while negative residuals indicate LST values lower than predicted. The standard deviation of the residuals from the training set ($\sigma_{\Delta T}$) was then computed and used to establish dynamic thresholds for residual-based anomaly detection.

As a result, a second set of anomaly masks was generated using these residual thresholds:

$$M_2^{\text{hot}} = \{(i, j) \mid \Delta T_{i,j} > k \cdot \sigma_{\Delta T}\} \tag{12}$$

$$M_2^{\text{cold}} = \{(i, j) \mid \Delta T_{i,j} < -k \cdot \sigma_{\Delta T}\} \tag{13}$$

where k is the threshold multiplier controlling detection sensitivity. For this study, we considered $k = 1.5$ as a moderate detection threshold. This choice balances both sensitivity and specificity.

Final anomaly cores were defined as the intersection of statistical and residual-based anomalies:

$$C^{\text{hot}} = M_1^{\text{hot}} \cap M_2^{\text{hot}} \tag{14}$$

$$C^{\text{cold}} = M_1^{\text{cold}} \cap M_2^{\text{cold}} \tag{15}$$

where C^{hot} and C^{cold} represent the refined hot and cold anomaly cores, respectively.

Following the intersection of statistical and residual-based masks, mathematical morphology operations were applied to merge fragmented anomaly pixels and smooth irregular boundaries. Let B_r denote a disk-shaped structuring element of radius r pixels.

Binary closing $(C \oplus B_r) \ominus B_r$ with $r = 3$ filled small internal gaps, where $\oplus$ denotes dilation and $\ominus$ denotes erosion:

$$C^{\text{closed}} = (C \oplus B_3) \ominus B_3 \tag{16}$$

Subsequent dilation with B_4 merged spatially proximate anomalies:

$$C^{\text{dilated}} = C^{\text{closed}} \oplus B_4 = \{z \mid (\hat{B}_4)_z \cap C^{\text{closed}} \neq \emptyset\} \tag{17}$$

where $\hat{B}_4$ denotes the reflection of B_4 and subscript z indicates translation. This established an agglutination distance of 4 pixels.

Binary opening $(C \ominus B_r) \oplus B_r$ with $r = 4$ smoothed boundaries:

$$C^{\text{opened}} = (C^{\text{dilated}} \ominus B_4) \oplus B_4 \tag{18}$$

Connected components smaller than threshold $\tau = 1$ pixel were removed via connected component labeling:

$$C^{\text{unified}} = \{c \in \text{Connected Components}\ (C^{\text{opened}}) \mid |c| \geq \tau\} \tag{19}$$

where $|c|$ denotes pixel count in component c. Components were identified using 8-connectivity (Moore neighborhood). These operations follow standard mathematical morphology methods (Serra, 1982; Haralick et al., 1987; Rosenfeld & Pfaltz, 1966; Samet & Tamminen, 1988), producing unified cores ($C^{\text{hot}}_{\text{unified}}$, $C^{\text{cold}}_{\text{unified}}$) with coherent spatial structure.

This dual-stage intersection ensures that identified anomalies are both statistically extreme in absolute terms and thermally unexpected given their land cover characteristics. This methodology, therefore, distinguishes spatial and thermally relevant IUHIs and IUCIs from mere temperature variations associated with different surface types and their naturally heterogeneous energy balances.

Dual-metric System

The relevance of a thermal anomaly for urban planning, public health, and heat mitigation is determined not only by its core intensity but also by how extensively its thermal conditions propagate into the surrounding urban fabric (Norton et al., 2015; Bowler et al., 2010). A small, isolated anomaly, for instance, has fundamentally different implications than one whose thermal signature extends across multiple city blocks.

To quantify these two distinct characteristics, that is, the intensity of the core itself and the extent of its spatial influence, the Tocantins Framework serves as a dual-metric system, accounting for the Severity Score (SS) and the Impact Score (IS).

Severity Score

The Severity Score (SS) quantifies the overall significance of the anomaly core by integrating its thermal intensity and its spatial area. This metric is internally focused on the core's properties.

SS integrates two components: Thermal Intensity (normalized temperature deviation) and Core Area (spatial extent of the anomaly core).

Thermal Intensity measures the normalized thermal deviation of the core:

$$\text{Thermal Intensity} = \frac{|\text{median}(\Delta T_C)|}{\sigma_{\Delta T}} \tag{20}$$

where ΔT_C represents residuals within the core region.

Core Area quantifies the spatial extent of the anomaly:

$$\text{Core Area} = n_{\text{core pixels}} \times (\text{Spatial Resolution})^2 \tag{21}$$

where $n_{\text{core pixels}}$ is the total count of pixels within the core region ($C^{\text{hot}}_{\text{unified}}$ or $C^{\text{cold}}_{\text{unified}}$) and Spatial Resolution is the sensor's pixel side length. Since this study utilizes data from Landsat 8, Spatial Resolution = 30 m.

These components are then integrated by applying logarithmic transformation to compresses scale and the preserving sign for anomaly type distinction. Positive SS indicates hot anomaly cores, negative indicates cool anomaly cores:

$$\text{SS} = \text{sign}(\text{median}(\Delta T_C)) \times \log(1 + \text{Thermal Intensity} \times \text{Core Area}) \tag{22}$$

Impact Score

The Impact Score (IS) quantifies the spatial extent and thermal intensity of the Extended Anomaly Zone (EAZ) surrounding an anomaly core. For this framework, we define the impact of an intra-urban thermal anomaly as the spatial reach and thermal magnitude of unexpectedly high (or low) temperatures extending outward from the anomaly core, quantified as the extent of the surrounding zone where observed temperatures exceed predictions from land cover spectral indices.

To capture this distinction, IS integrates three dimensions: the thermal intensity of the extended zone (Severity), its spatial reach (Area), and the smoothness of its thermal boundaries (Continuity). The latter distinguishes gradual thermal transitions, which suggest sustained anomalous conditions, from sharp discontinuities that may indicate measurement artifacts or isolated surface features.

To delineate Extended Anomaly Zones, potential EAZ pixels were identified by applying the residual threshold ($k \cdot \sigma_{\Delta T}$) to all non-core pixels:

$$\text{EAZ}^{\text{potential, hot}} = \{(i, j) \mid \Delta T_{i,j} > k \cdot \sigma_{\Delta T}\} \setminus C^{\text{hot}}_{\text{unified}} \tag{23}$$

This identifies all pixels exhibiting thermally unexpected conditions while excluding the core itself to separate the extended zone from the anomaly origin.

Connected component analysis was applied to the union of cores and potential EAZ pixels ($C^{\text{hot}}_{\text{unified}} \cup \text{EAZ}^{\text{potential, hot}}$) using 8-connectivity. Only connected components containing at least one core pixel were retained:

$$L = \text{Label}(C^{\text{hot}}_{\text{unified}} \cup \text{EAZ}^{\text{potential, hot}}, \text{connectivity} = 8) \tag{24}$$

$$L^{\mathrm{core}} = \{l \in L \mid \exists (i,j) \in C^{\mathrm{hot}}_{\mathrm{unified}}, L_{i,j} = l\} \tag{25}$$

This spatial connectivity requirement ensures that Extended Anomaly Zones are physically anchored to anomaly cores rather than representing unrelated thermal variations elsewhere in the urban area.

The Extended Anomaly Zone was defined as:

$$\mathrm{EAZ}^{\mathrm{hot}} = \{(i,j) \mid L_{i,j} \in L^{\mathrm{core}}\} \setminus C^{\mathrm{hot}}_{\mathrm{unified}} \tag{26}$$

Extended Anomaly Zones were smoothed using binary closing followed by opening with B_1:

$$\mathrm{EAZ}^{\mathrm{hot}}_{\mathrm{refined}} = [(\mathrm{EAZ}^{\mathrm{hot}} \circ B_1) \bullet B_1] \tag{27}$$

where $\circ$ denotes closing and $\bullet$ denotes opening. These morphological operations remove small isolated pixels and smooth irregular boundaries that may result from sensor noise or edge effects. Analogous operations were performed for cold anomalies.

Similar to the Severity Score calculation, Severity measures the normalized thermal intensity of the Extended Anomaly Zone:

$$\mathrm{Severity} = \frac{|\mathrm{median}(\Delta T_{\mathrm{EAZ}})|}{\sigma_{\Delta T}} \tag{28}$$

where ΔT_{EAZ} represents residuals within the Extended Anomaly Zone, rather than within $C^{\mathrm{hot}}_{\mathrm{unified}}$ or $C^{\mathrm{cold}}_{\mathrm{unified}}$ cores. Normalization by $\sigma_{\Delta T}$ standardizes intensity across different time periods and atmospheric conditions, enabling temporal comparisons.

Area quantifies spatial extent:

$$\text{Area}_{\text{EAZ}} = n_{\text{EAZ pixels}} \times (\text{Spatial Resolution})^2 \tag{29}$$

where $n_{\text{EAZ pixels}}$ is the total count of pixels within the Extended Anomaly Zone and Spatial Resolution = 30 m for Landsat data acquired for this study.

Larger areas indicate that anomalous thermal conditions persist over greater distances from the core, suggesting broader potential exposure or more extensive underlying causes.

Continuity measures boundary smoothness using spatial gradient magnitude:

$$\text{Continuity} = \frac{1}{1 + \bar{G}_{\text{boundary}}} \tag{30}$$

where $\bar{G}_{\text{boundary}}$ is the mean gradient at the anomaly boundary (inner and outer edges), calculated as $G_{i,j} = \sqrt{(\partial \Delta T/\partial x)^2 + (\partial \Delta T/\partial y)^2}$. Sharp gradients indicate abrupt thermal transitions characteristic of isolated surface features or image artifacts, yielding low continuity values. Smooth gradients suggest sustained thermal conditions extending across space, yielding high continuity values and contributing to higher impact scores.

The Impact Score integrates these components multiplicatively:

$$\text{IS} = \text{sign}(\text{median}(\Delta T_{\text{EAZ}})) \times \log(1 + \text{Severity} \times \text{Area} \times \text{Continuity}) \tag{31}$$

The multiplicative structure reflects that high impact requires the simultaneous presence of all three factors: thermal intensity, spatial extent, and smooth propagation. An anomaly with high severity but a small area, or a large area but low severity, will yield lower impact scores than one exhibiting both characteristics together. Similarly to the Severity Score, logarithmic transformation compresses the scale, preventing dominance by extreme outliers, and sign preserves anomaly type.

Code and Data Availability

The complete implementation of the Tocantins Framework is available as open-source software under the MIT License at `https://github.com/EcoAcao-Brasil/tocantins-framework`. The framework can be installed via PyPI (`pip install tocantins-framework`) and includes comprehensive documentation, example workflows, and all processing scripts used in this study (Borges, 2025). Landsat imagery used for the Palmas case study can be accessed through the USGS Earth Explorer platform (`https://earthexplorer.usgs.gov/`).

Results

When applied to the Landsat 8 composite from the first semester of 2025 for Palmas, Tocantins, Brazil, the Random Forest regression model achieved strong predictive performance in modeling the relationship between spectral indices and land surface temperature. The model achieved an R^2 score of 0.8023 (RMSE = 1.1612°C), indicating that approximately 80% of the variance in LST within the Palmas urban area could be explained by the combination of NDVI, NDWI, NDBI, and NDBSI. The residual standard deviation of 1.1612°C established the baseline for subsequent anomaly detection thresholds, with the threshold multiplier $k = 1.5$ corresponding to thermal deviations exceeding ±1.74°C from predicted values based on local spectral characteristics.

The framework identified 103 thermal anomalies across the Palmas urban area, comprising 76 Intra-Urban Heat Islands (IUHIs) and 27 Intra-Urban Cool Islands (IUCIs). These anomalies collectively covered 30.42 km^2 of urban surface, distributed as 26.38 km^2 in hot anomaly cores and 4.04 km^2 in cold anomaly cores. Hot anomalies exhibited substantially larger mean core areas (347,044.74 m^2 ± 445,198.32 m^2) compared to cold anomalies (149,766.67 m^2 ± 178,523.45 m^2), suggesting that thermally excessive conditions tend to aggregate over larger contiguous areas

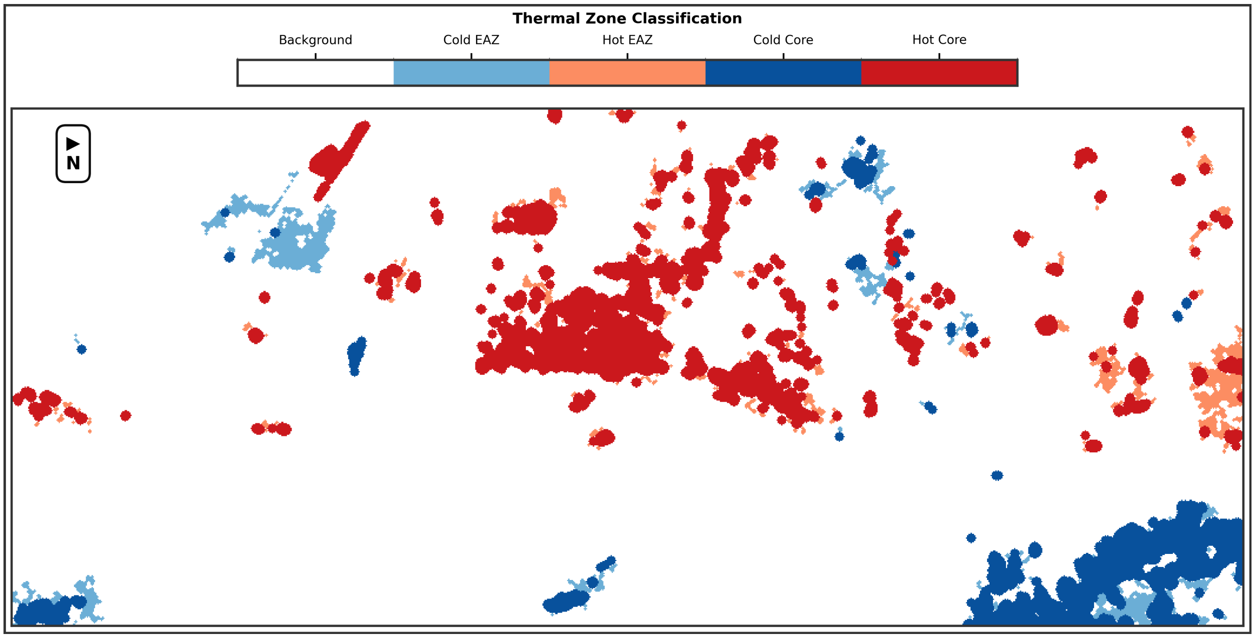

Figure 3: Map of thermal zone classification within the selected urban polygon. EAZ stands for Extended Anomaly Zones.

within the urban fabric. Conversely, cold anomalies demonstrated notably larger mean Extended Anomaly Zone areas (268,800 m^2 ± 412,633.87 m^2) compared to hot anomalies (79,661.84 m^2 ± 154,287.93 m^2), indicating that cool islands, while having smaller extreme cores, exhibit more extensive underlying thermal anomalousness extending beyond their most visible manifestation.

Figure 3 presents the spatial distribution of thermal zone classifications across the Palmas urban polygon. The map reveals the geographic extent of anomaly cores and their associated Extended Anomaly Zones, illustrating how thermal anomalousness manifests across the urban landscape. Certain anomalies present as isolated cores with minimal surrounding anomalous conditions, where the statistically extreme pixels constitute the entirety of detectable thermal deviation. In contrast, other anomalies reveal substantial additional extent beyond their cores, indicating that extreme values alone underestimate the true spatial scale of the phenomenon. A notable feature of the framework is that multiple anomaly cores can share the same Extended Anomaly Zone when they are spatially proximate and connected through contiguous thermally anomalous pixels.

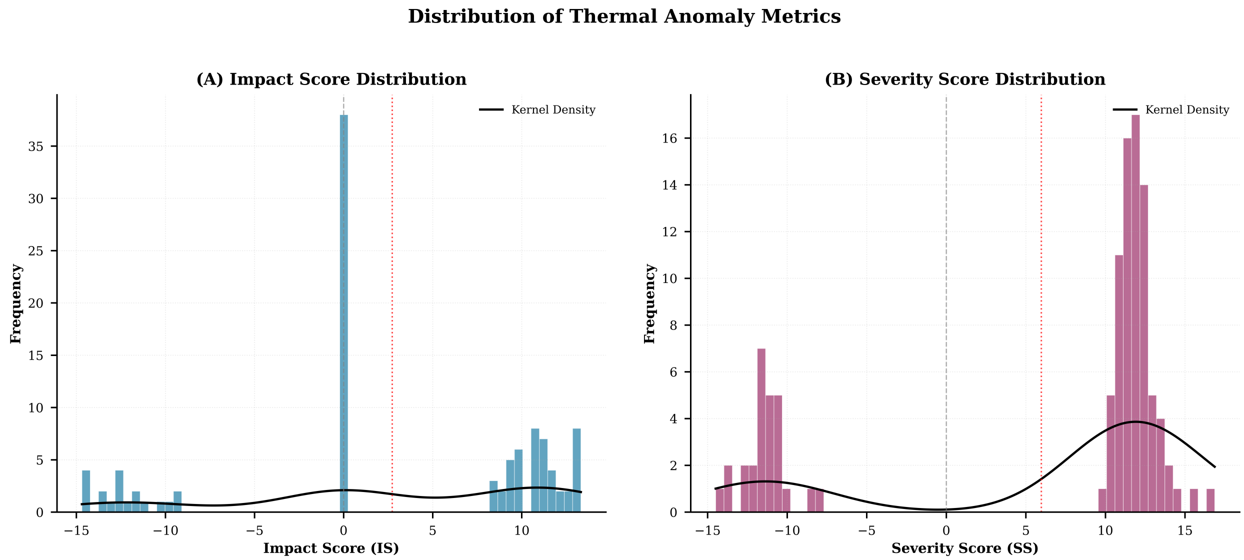

Figure 4: Frequency distributions of Impact Score (IS) and Severity Score (SS) for identified thermal anomalies.

Impact Scores for the 103 detected anomalies ranged from −14.69 to 13.32 (mean absolute value: 7.11 ± 4.82), while Severity Scores spanned from −14.49 to 16.87 (mean absolute value: 11.80 ± 2.87). However, 38 anomalies (36.9% of the total) exhibited Impact Scores of zero, indicating that while these locations met the dual criteria for anomaly core classification, they existed as isolated extremes without substantial surrounding zones of thermal anomalousness. Among these zero-IS anomalies, 26 were hot anomalies (34.2% of all IUHIs) and 12 were cold anomalies (44.4% of all IUCIs).

The distribution of Impact Scores and Severity Scores across all 103 anomalies reveals distinct patterns (Figure 4). When restricting analysis to the 65 anomalies with non-zero Impact Scores, the relationship between the absolute values of both metrics shows weak positive correlations that vary by anomaly type (Figure 5). For cold anomalies, the coefficient of determination is $R^2 = 0.158$, indicating that 15.8% of the variance in Impact Score can be explained by Severity Score. Hot anomalies exhibit a slightly stronger relationship (R^2 = 0.211, or 21.1% explained variance), while the composite relationship across the module of all anomalies yields R^2 = 0.154 (15.4% explained variance). These weak to moderate correlations confirm that the two metrics capture substantially different and complementary aspects of thermal anomaly phenomena. The fact that 78.9% to 84.6% of Impact Score variance remains unexplained by Severity Score validates the dual-metric approach, demonstrating that anomalies with high core intensity are not necessarily embedded within extensive zones of thermal anomalousness, and vice versa.

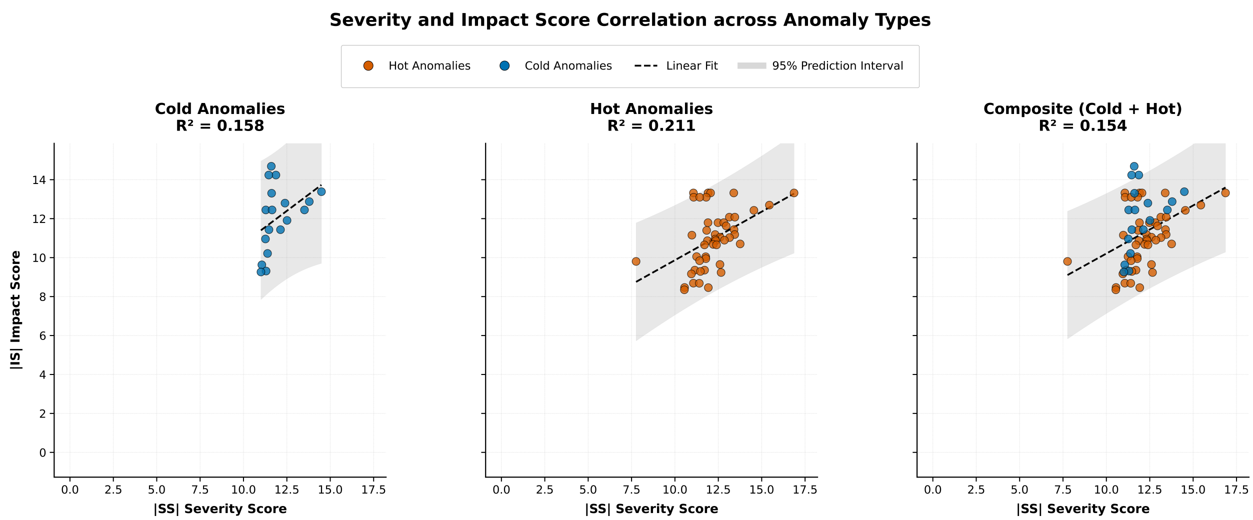

Figure 5: Relationship between absolute Severity Score and absolute Impact Score across cold, hot, and composite thermal anomalies exhibiting non-zero IS values.

Discussion and Conclusion

The Tocantins Framework addresses the absence of standardized metrics for intra-urban thermal anomalies. While Urban Heat Island studies employ established methodologies (Oke, 1982; Stewart & Oke, 2012), micro-urban thermal variations have lacked analytical rigor. The dual-metric system operationalizes core intensity (Severity Score) and thermo-spatial extent (Impact Score) as independent, quantifiable dimensions.

The Random Forest model achieved $R^2 = 0.8023$, consistent with remote sensing studies relating spectral indices to LST (Guha et al., 2018; Sekertekin et al., 2016). Residual-based detection distinguishes pixels that are unexpectedly hot or cold from those that are simply hot or cold due to material properties. This framework's central contribution is separating spectral expectation from thermal reality in the asessment of intra-urban heat and cool islands.

The weak correlation between metrics ($R^2 = 0.154$ composite, 0.158 cold, 0.211 hot) validates the dual-metric design. If severity predicted extent, one metric would suffice. The independence confirms different physical mechanisms. High-severity isolated anomalies (36.9% with IS = 0) represent localized surface modifications, which pose localized risks but lack neighborhood-scale impact (Norton et al., 2015).

Conversely, moderate-severity anomalies within Extended Anomaly Zones indicate systemic patterns where significant areas exhibit thermal behavior inconsistent with spectral properties. The 43 cores (41.7%) grouped into 18 shared EAZs reveal hierarchical thermal structure: neighborhood-scale regimes hosting multiple localized peaks. These require comprehensive neighborhood interventions rather than site-specific modifications (Harlan et al., 2006).

The hot-cold asymmetry is physically grounded. Hot anomalies form larger cores (347,045 m^2 mean) because heat accumulates in high-thermal-mass materials and concentrated land uses (Grimmond et al., 1991). Cold anomalies develop larger EAZs (268,800 m^2 mean) because cooling mechanisms such as evapotranspiration and shading propagate through air movement and radiation geometry (Bowler et al., 2010; Spronken-Smith & Oke, 1998; Cao et al., 2010). The framework captures this physical distinction quantitatively.

While Landsat data enables 40-year retrospective analysis and global cross-city comparison impossible with modern, higher-resolution sensors, its 30-meter resolution imposes limitations on detecting hyperlocal thermal features at very fine scales, potentially missing building-level variations that may contribute to microclimate regulation (Chen et al., 2022). This constraint is inherent to open-source satellite imagery and represents a fundamental trade-off: fine-scale spatial detail versus temporal depth and global accessibility.

However, its resolution remains adequate for neighborhood-scale anomaly detection and district planning interventions, which constitute the primary scale of urban heat mitigation policy. Additionally, Landsat's 16-day revisits characterize observed anomalies as persistent rather than transients.

This way, the Tocantins Framework characterizes persistent structural thermal patterns rather than ephemeral fluctuations, appropriate for planning applications that address long-term urban form rather than transient weather events.

As for the threshold $k = 1.5$ (1.74°C residual deviation for Palmas), it balances sensitivity and specificity. Lower values risk false positives; higher values miss emerging issues. The 1.74°C magnitude matches existing literature and study of temperature deviations in urban settings (Chang et al., 2007; Bowler et al., 2010). The modular design permits threshold adjustment for different contexts.

Morphological operations transform pixel detections into spatial objects. Closing (r = 3) merges fragments, dilation (r = 4, 120 m at Landsat resolution) agglutinates proximate anomalies sharing mechanisms, opening (r = 4) smooths boundaries (Serra, 1982; Soille, 2003). These parameters are defensible and adjustable.

The open-source implementation (PyPI: tocantins-framework) removes barriers between methodology and application (Borges, 2025). Practitioners apply the framework without specialized remote sensing expertise. Integration with standard GIS workflows enables incorporation into existing planning processes (Rey et al., 2015).

Future work should apply the framework to multi-year archives, tracking anomaly evolution in response to development, policy, or climate. Cross-city comparison would identify urban form typologies associated with thermal patterns. Integration with 3D building geometry and demographics would enable causal analysis (Li et al., 2024; Hsu et al., 2021).

The framework advances from descriptive heat mapping to quantitative anomaly characterization. The dual metrics distinguish core intensity from spatial propagation, enabling prioritization by local severity and neighborhood impact. This provides standardized tools for evidence-based urban heat mitigation.

Acknowledgments

The authors would like to express their sincere gratitude to all members of EcoAção Brasil for their invaluable support, critical feedback, and collaborative spirit.

We thank Anna Vitoria Mauricio for her outstanding leadership of the Marketing and Communications team, who wholeheartedly shared our work and instigated public awareness of this research. We also express our gratitude to Melissa Afonso Correia e Silva, Debora Cristine dos Santos Borges, and Giovanna Vitória de Godoi Augusto for their commitment to this effort. We specifically acknowledge Debora dos Santos Borges for her support in conceptualizing this paper's figures under the orientation of co-author Johari.

We appreciate the thoughtful support from the Applied Research team, under the remarkable management of Lucas Rocha Avelino, which has already begun evaluating the applications of the Tocantins Framework for EcoAção Brasil's upcoming AI model for urban planning. We also thank Diego Jose Figarella Urbaneja and Luiz Filipe Seabra de Marco for their support in developing this prototype.

Furthermore, we acknowledge the technical support provided by Giovanna Vitória de Godoi Augusto and Alexandre Costa dos Santos, with special mention to the development of EcoAção Brasil's website.

This research was made possible by the open-access Landsat 5, 7, 8, and 9 data archives, provided by the U.S. Geological Survey (USGS), and the computational resources of the Google Earth Engine platform.

This work was supported by The Earth Foundation through The Earth Prize 2025, awarded to the first author, Isaque Carvalho Borges, the founder, president, and lead researcher of the Pure Research and Applied Research teams of EcoAção Brasil.

References

Aniello, C., K. Morgan, A. Busbey, & L. Newland, (1995). Mapping micro-urban heat islands using LANDSAT TM and a GIS. *Computers & Geosciences* 21(8), 965–969.

Aram, F., E. Higueras García, E. Solgi, & S. Mansournia, (2019). Urban green space cooling effect in cities. *Heliyon* 5(4), e01339.

Aucoin, S., A. Briand, B. Duval, & Z. Qudsi, (2022). Micro-urban heat islands in the City of Montreal. *McGill Science Undergraduate Research Journal* 17(1), 58–63.

Borges, Isaque Carvalho, (2025). Tocantins framework: A python library for assessment of intra-urban thermal anomaly.

Bowler, Diana E., Lisette Buyung-Ali, Teri M. Knight, & Andrew S. Pullin, (2010). Urban greening to cool towns and cities: A systematic review of the empirical evidence. *Landscape and Urban Planning* 97(3), 147–155.

Cao, X., A. Onishi, J. Chen, & H. Imura, (2010). Quantifying the cool island intensity of urban parks using ASTER and IKONOS data. *Landscape and Urban Planning* 96(4), 224–231.

Chang, C.-R., M.-H. Li, & S.-D. Chang, (2007). A preliminary study on the local cool-island intensity of Taipei city parks. *Landscape and Urban Planning* 80(4), 386–395.

Chen, P., (2024). Inequality in heat: The role of spatial patterns of urban green infrastructure. *Urban Climate* 53, 101820.

Chen, Y., B. Shan, & X. Yu, (2022). Study on the spatial heterogeneity of urban heat islands and influencing factors. *Building and Environment* 208, 108604.

Deng, Yue, Changshan Wu, Manchun Li, & Rong Chen, (2018). RNDSI: A ratio normalized difference soil index for remote sensing of urban/suburban environments. *International Journal of Applied Earth Observation and Geoinformation* 65, 65–77.

Gao, Bo-Cai, (1996). NDWI—a normalized difference water index for remote sensing of vegetation liquid water from space. *Remote Sensing of Environment* 58(3), 257–266.

Grimmond, C. S. B., H. A. Cleugh, & T. R. Oke, (1991). An objective urban heat storage model and its comparison with other schemes. *Atmospheric Environment. Part B. Urban Atmosphere* 25(3), 311–326.

Guha, S., H. Govil, & S. Mukherjee, (2018). Dynamic analysis and ecological evaluation of urban heat islands in raipur city, india. *Journal of Applied Remote Sensing* 11(3), 036020.

Haralick, Robert M., Stanley R. Sternberg, & Xinhua Zhuang, (1987). Image analysis using mathematical morphology. *IEEE Transactions on Pattern Analysis and Machine Intelligence* 9(4), 532–550.

Harlan, S. L., A. J. Brazel, L. Prashad, W. L. Stefanov, & L. Larsen, (2006). Neighborhood microclimates and vulnerability to heat stress. *Social Science & Medicine* 63(11), 2847–2863.

Hsu, A., G. Sheriff, T. Chakraborty, & D. Manya, (2021). Disproportionate exposure to urban heat island intensity across major US cities. *Nature Communications* 12, 2721.

IBGE, (2019). Ibge - Áreas urbanizadas. Accessed: 2025-08-06.

Li, Y., J. C. Svenning, W. Zhou, S. Wang, S. Tong, Q. Ma, X. Wang, R. Zeng, X. Li, Y. Liu, X. Li, Y. Zhang, Z. Li, H. Guo, & X. Li, (2024). Green spaces provide substantial but unequal urban cooling globally. *Nature Communications* 15, 7108.

Mazzone, A., E. De Cian, E. de Paula, A. Ferreira, & R. Khosla, (2024). Understanding thermal justice and systemic cooling poverty from the margins: Intersectional perspectives from Rio de Janeiro. *Local Environment* 29(8), 1026–1043.

Norton, Briony A., Andrew M. Coutts, Stephen J. Livesley, & Nicholas S. G. Williams, (2015). Planning for cooler cities: A framework to prioritise green infrastructure to mitigate high temperatures in urban landscapes. *Landscape and Urban Planning* 134, 127–138.

Oke, T. R., (1982). The energetic basis of the urban heat island. *Quarterly Journal of the Royal Meteorological Society* 108(455), 1–24.

Onishi, A., X. Cao, T. Ito, F. Shi, & H. Imura, (2010). Evaluating the potential for urban heat-island mitigation by greening parking lots. *Urban Forestry & Urban Greening* 9(4), 323–332.

Rey, Sergio J., Luc Anselin, Xun Li, Robert Pahle, Jason Laura, Wenwen Li, & Julia Koschinsky, (2015). PySAL: A Python library of spatial analytical methods. *The Review of Regional Studies* 37(1), 5–27.

Rosenfeld, Azriel & John L. Pfaltz, (1966). Sequential operations in digital picture processing. *Journal of the ACM* 13(4), 471–494.

Samet, Hanan & Markku Tamminen, (1988). Efficient component labeling of images of arbitrary dimension represented by linear bintrees. *IEEE Transactions on Pattern Analysis and Machine Intelligence* 10(4), 579–586.

Sekertekin, A., S. H. Kutoglu, & S. Kaya, (2016). Evaluation of spatio-temporal variability in Land Surface Temperature: A case study of Zonguldak, Turkey. *Environmental Monitoring and Assessment* 188(1), 30.

Serra, Jean, (1982). *Image Analysis and Mathematical Morphology*. Academic Press, London.

Soille, Pierre, (2003). *Morphological Image Analysis: Principles and Applications*. Springer, Berlin, 2nd ed.

Spronken-Smith, R. A. & T. R. Oke, (1998). The thermal regime of urban parks in two cities with different summer climates. *International Journal of Remote Sensing* 19(11), 2085–2104.

Stewart, I. D. & T. R. Oke, (2012). Local climate zones for urban temperature studies. *Bulletin of the American Meteorological Society* 93(12), 1879–1900.

Tucker, Compton J., (1979). Red and photographic infrared linear combinations for monitoring vegetation. *Remote Sensing of Environment* 8(2), 127–150.

United States Geological Survey, (2022). Landsat collection 2 level-2 science products. Accessed: 2024-10-17.

Wang, Y., S. Di Sabatino, A. Martilli, Y. Li, M. S. Wong, E. Gutiérrez, & P. W. Chan, (2017). Impact of land surface heterogeneity on urban heat island circulation and sea-land breeze circulation in Hong Kong. *Journal of Geophysical Research: Atmospheres* 122, 4332–4352.

Wong, N. H. & C. Yu, (2005). Study of green areas and urban heat island in a tropical city. *Habitat International* 29(3), 547–558.

Yang, X., Y. Li, Z. Luo, & P. W. Chan, (2017). The urban cool island phenomenon in a high-rise high-density city and its mechanisms. *International Journal of Climatology* 37, 890–904.

Zha, Y., J. Gao, & S. Ni, (2003). Use of normalized difference built-up index in automatically mapping urban areas from TM imagery. *International Journal of Remote Sensing* 24(3), 583–594.